Modeling considerations for imaging with a standard metal detector[*]

Pascal Druyts, Lionel Merlat[†], Marc Acheroy

Signal Image Center, Royal Military Academy
Avenue de la Renaissance, 30 – 1000 Brussels, Belgium
Pascal.Druyts@elec.rma.ac.be, lmerlat@elec.rma.ac.be, Marc.Acheroy@elec.rma.ac.be

ABSTRACT

A standard pulsed induction metal detector is used to image buried metallic objects by scanning an area of interest. It is shown that, under specific hypotheses, the output image is the result of the convolution of a target function with a kernel depending on the incident magnetic field. Several hypotheses are considered, leading to different kernel shapes and different interpretations of the target function. As the detector imaging function is a low-pass filter, shape's details spread out and the resulting raw images are blurred. Since a high-pass restoration filter must be used to deconvolve the raw images, care must be taken to avoid a strong amplification of noise. The imaging filter is computed using a numerical simulation of the incident magnetic field. Finally, the restoration filter is computed using the Wiener approach. Results are shown for a couple of metallic pieces.

Keywords: electromagnetic induction imaging, image restoration, buried landmine detection.

NOTATIONS

Symbol	Description	Symbol	Description
s	Laplace variable (derivation operator).	$\vec{J}$	current density
j	complex unity: $j^2 = -1$	V	electric scalar potential
ω	pulsation or Fourrier transform variable	$\vec{A}$	magnetic vector potential
a	Scalar	V^*	magnetic scalar potential
$\vec{a}$	3D column vector or equivalently a first order 3D column tensor	$\vec{H}_c$ $\vec{H}_{c0}$ $\vec{H}_t$	respectively the magnetic field generated by the coil, the magnetic field generated by the coil for a unit current and the magnetic field scattered by the target. The same subscript convention holds for the other fields and potentials.
a_i	component of the vector $\vec{a}$	$V_c(s)$	time varying voltage induced in the detector coil
$\vec{a}^T$	3D line vector or equivalently, first order 3D line tensor resulting from the transposition of $\vec{a}$.	V_m	output of the detector; it results from the evaluation of $V_c(s)$ by means of time integration
$\ddot{a}$	second order 3D tensor	$\ddot{M}(s)$	magnetic polarizability
a_{ij}	components of the tensor $\ddot{a}$	$\ddot{\Gamma}$	evaluated (by the metal detector) magnetic polarizability
$\ddot{1}$	identity tensor whose components are δ_{ij}	$\vec{m}(s)$	dipolar moment
$\vec{1}_{\vec{a}}$ or $\vec{1}_a$	unit vector in the direction of $\vec{a}$ $\vec{1}_{\vec{a}} = \vec{a}/\lVert\vec{a}\rVert$.	$\vec{\nabla}$	Nabla operator $\vec{\nabla} = (\dfrac{\partial}{\partial x}, \dfrac{\partial}{\partial y}, \dfrac{\partial}{\partial z})$.
$\vec{a}.\vec{b}$	scalar product of $\vec{a}$ and $\vec{b}$	Δ	Laplacien operator $\Delta\varphi = \dfrac{\partial^2\varphi}{\partial x^2} + \dfrac{\partial^2\varphi}{\partial y^2} + \dfrac{\partial^2\varphi}{\partial z^2}$
$\vec{a}\times\vec{b}$	vector product of $\vec{a}$ and $\vec{b}$	$\vec{r}_c$	gravity center of the metal detector coil
$\vec{a}\vec{b}$	dyadic or external product $\vec{c} = \vec{a}\vec{b}$ where $c_{ij} = a_i b_j$	$\vec{r}_t$	gravity center of a target
$\ddot{a}\vec{b}$ $\ddot{a}\vec{b}$ $\vec{b}^T\ddot{a}$	tensor products whose components are $a_{ij}b_{jk}$, $a_{ij}b_j$ and $a_{ij}b_i$ respectively	$\vec{R}$	an integration variable. It appears always in integrals together with one of the three following line, surface or volume element
$\vec{H}$	magnetic field	$d\vec{l}$	line element

$\vec{B}$	magnetic induction field	$d\vec{S}$	surface element
$\vec{E}$	electric field	dV	volume element
$\vec{D}$	electric displacement field	X_t X_c	Where X is $\vec{R}$, $\vec{dl}$, $d\vec{S}$ or dV indicates whether the quantity refers to the MD coil or the target
$a(t) * b(t)$	Is the convolution of a and b		

1   INTRODUCTION

The metal detector (MD) is widely used for the detection of buried metallic items. Its application field spreads from classical treasure hunting to archeology and civil engineering. Since World War II, militaries and NGOs are commonly using it for demining operations [1, chap. 1].

Common MD's rely on single coil, or a set of coils, illuminating the ground with a time varying magnetic field. Electromotive forces are induced in the conductive materials and in turn produce eddy currents. These currents induce a secondary (very weak) magnetic field, which is picked up by a receiving coil. The secondary field is converted into a signal, which is up to now only little processed, to finally trigger an audio warning.

Although MDs' performances have been slightly increased since WWII, such as in the detection depth or the ground rejection, they still have poor discrimination capabilities. Especially in the mine detection context, it should be kept in mind that a MD is only sensitive to conductive and/or magnetic materials, and not an explosive products. Because most of the mines contain at least a minimum of metal, these detectors are able to localize them. Therefore, it turns out that the detector doesn't only trigger on mines but also on metal scraps, bullet casings and other battlefield debris, barbed wires, etc.. This yields a high false alarm rate (up to 999/1000). Furthermore, each alarm given by the MD must be manually checked out by probing the ground with a bayonet and the source of the alarm must be dug out. This is the main reason why demining is dramatically slow.

Some efforts have been initiated for a couple of years to improve the MD in order to reduce its false alarm rate. Several tracks are followed, which are based either on new technologies (multi-coils, multi-frequency induction mode [2], etc.) or on signal processing (fingerprint analysis [4], imaging, etc.). The work reported in this paper belongs to the second category.

Our aim is to provide the operator with valuable images in which typical metallic objects may be recognized and possibly, associate to some burying depth information. Metallic objects of interest are both parts of mines such as a firing pin or a metal strap, and (parts of) non-mine objects such as shells, cartridges, and barbed wire. In some cases, the image will allow the user to conclude with certainty if the object is a mine or not. In favorable circumstances (very characteristic objects, close to the surface, etc.), it could even be possible to identify the type of mine or non-mine object. In other cases, if the image is not sharp enough (object too small, too deeply buried, too complex, etc.) or if the observed shapes are not discriminant enough, it will not be possible to conclude with certainty whether the object is a mine or not. In this last case, it would be necessary to excavate the object and treat it like a mine. The image could however still be useful for adapting the excavation task. Images could thus be useful to speed up the demining by reducing the false alarm rate and also to increase the safety of the operator by providing complementary information about the object such as its burying depth, volume, orientation, a list of possible objects etc. Even if this complementary information is not 100% reliable, it could be quite valuable when compared to a blind prodding and excavation.

Images are the result of a 2D scan. The pathway does not need to follow a regular grid but this eases the post processing. There are several sources of blurring. On the emitter side, the detector generates a magnetic field which spreads like a bunch. This magnetic field induces eddy currents which may extend in regions of the target where the field generated by the emitting coil was null. The field generated by those eddy currents on its turn spreads like a bunch. Finally, on the receiver side, the detector integrates the flux through its coil, which presents a large section. If the targets of interest were larger than the detector footprint, raw images would reproduce the sharp details. Unfortunately targets of interest are much smaller (typically a few cm or less) than the detector footprint (typically, a mean diameter of 25 cm). A post-processing is thus required to enhance the image sharpness in order to make them interpretable by the operator. This de-blurring implies a strong amplification of the high frequencies of the signal that were attenuated by the imaging process. Care must be taken to avoid strong noise amplification. We will show that under specific hypothesis the imaging process may be modeled by means of a convolution filter. A Wiener filter [5] may then be used to restore the image taking into account the characteristics of the noise and of the imaging filter.

This paper is organized as follows. In section 2, the metal detector operation principle is presented. The interactions between the sensor and the targets are highlighted from a physical point of view. In section 3 a number of target models are developed. The real targets that may be represented by each developed model is also discussed. It will be shown that under some hypothesis, the imaging process may be modeled by the convolution of a *target function* with an *imaging kernel*. The interpretation of the target function and the shape of the imaging kernel will be discussed for each model

developed. Section 4 deals with the image restoration procedure. It presents the design of the Wiener restoration filter. Section 5 presents the experimental setup and shows results with targets of various sizes and shapes. Finally, section 6 concludes the discussion.

2   METAL DETECTOR

Generally speaking, a MD operates with either continuous wave (CW) or pulsed induction (PI) magnetic fields at low frequencies (audio band). The low frequency excitation allows for a deep penetration of the field into the ground. The wavelength is large when compared to the volume of interest and the targets are thus in the near field of the illuminator [1]. The propagation effects may therefore be neglected. The time varying magnetic field generated by the detector will induce eddy currents in conductive bodies. The eddy current evolution will be governed by the resistive and inductive characteristics of the path through which they flow. We may thus conclude that the only relevant parameters are the conductivity and magnetic permeability together with the target geometry. If a target is in the field of the detector, the detector answer will be influenced by the target shape, relative position and orientation, conductivity and magnetic permeability. The electrical permeability of the target and its surrounding is irrelevant.

The MD we use is a standard model and operates in PI mode [2] with a single coil. It generates a magnetic field of very short duration. After the primary field has vanished, the coil senses only the secondary field, which is generated by the eddy currents induced in the targets (Figure 1.a). In our case, the excitation current waveform is a saw tooth train with alternate sign (Figure 1.b). Its spectrum upper bound is mainly defined by the frequency components of the fast decreasing phase, which lasts for about 5 µs. Hence, the bandwidth amounts approximately 200 kHz. This complies with the above assumption of negligible propagation effects and the whole system can be modeled in the quasi-static magnetic regime. It should be noted that such a detector is not able to detect non-conductive targets even if they present a magnetic permeability contrast with their surrounding.

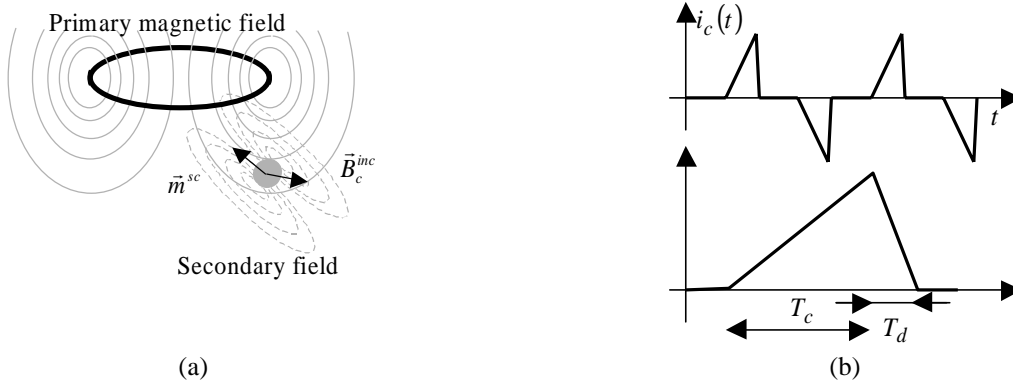| (a) | (b) |

Figure 1 – (a) A small target laid in the primary varying magnetic field back-scatters a secondary field. (b) Coil current waveform of the pulsed induction metal detector used. The lower view is a zoom on a single saw tooth of the train shown at the top. T_c is the charging period, whereas T_d is the fast discharging one.

The incident magnetic field induced at the point $\vec{r}$ by a horizontal coil located at the origin when driven by a current $I_c(s)$, where s is the Laplace variable, is (Biot Savart law) [7]:

$$\vec{B}_c(\vec{r}) = \frac{\mu_0 I_c}{4\pi} \oint_{coil} \frac{d\vec{l}_c \times \vec{1}_{R_c-\vec{r}}}{\left\|\vec{R}_c - \vec{r}\right\|^2}$$

(1)

This expression may be used to compute the magnetic field generated by a specific metal detector if the geometry of its coil is known. In practice, the field is computed on a 3D lattice by means of a numerical integration procedure.

With the adopted notations, $\vec{B}_{c0}$ is defined as the magnetic incident field per unit current ($\vec{B}_{c0} = \vec{B}_c / I_c$).

The voltage induced into the coil results from the Lentz law ($EMF = -d\phi/dt$). As there is no current flowing into the coil during the measurement phase, the total voltage measured across the coil is due to the magnetic field back-scattered by the target.

$$V_c(s) = s \int_{S_c} \vec{B}_t(\vec{R}_c, s) d\vec{S}_c$$

(2)

This may also be written using the magnetic vector potential as a function of the current density in the target $\vec{J}_t$:

$$\vec{A}_t(\vec{r},s) = \frac{\mu}{4\pi} \int_{V_t} \frac{\vec{J}_t(\vec{R}_t,s)}{\|\vec{r} - \vec{R}_t\|} dV_t \tag{3}$$

$$V_c(s) = s \oint_{coil} \vec{A}_t(\vec{R}_c,s) d\vec{l}_c = \frac{\mu s}{4\pi} \oint_{coil} d\vec{l}_c \cdot \int_{V_t} \frac{\vec{J}_t(\vec{R}_t,s)}{\|\vec{R}_c - \vec{R}_t\|} dV_t \tag{4}$$

Equation 4 may be rewritten by permuting the order of integration:

$$V_c(s) = s \int_{V_t} \vec{J}_{t\arg et}(\vec{R}_t,s) \cdot \vec{A}_c^0(\vec{R}_t) dV_t \tag{5}$$

where

$$\vec{A}_c^0(\vec{r}) = \frac{\mu}{4\pi} \oint_{coil} \frac{1}{\|\vec{R}_c - \vec{r}\|} d\vec{l}_c \tag{6}$$

is the magnetic vector potential corresponding to a unit current in the coil.

Equation (5) is an expression of the reciprocity theorem [8] and may be used to compute the voltage induced in the coil by integrating over the target volume V_t.

The advantage of this formulation is that the voltage induced in the coil by any target may be computed once the current density in the target is known without computing the magnetic field generated by the currents and without integrating the flux on the (possibly complex) shape of the coil.

The voltage expressed by (5) is a time dependent function. An evaluation function that operates on that time varying voltage to produce a scalar measurement is implemented inside the detector. This evaluation function is a linear operator which calculates some kind of averaging on a given time window:

$$V_m = O\{V_c(s)\} \tag{7}$$

The signal V_m is then further processed to produce the audio alarm. This last processing is not considered in this paper because we use as input of the signal processing algorithms the signal V_m, which we call the metal detector output. The detector we use provides this signal through a numerical output interface. Obviously, when going from $V_c(s)$ to V_m, valuable information about the target signature is lost but we don't know of any commercial metal detector that provides access to $V_c(s)$.

3   TARGET MODELS

1   Introduction

We have shown in the previous section that the only parameters influencing the metal detector output are the magnetic permeability and electrical conductivity. Therefore, the general inverse problem uses as input the answer of the metal detector and produces a 3D image of the conductivity and permeability distributions of the underground. This would be a very useful information, as conductive or magnetic targets would appear sharply and well contrasted. The inverse problem has however an infinite number of solutions (ill-posed problem). This is due to the fact that a vector of characteristics (conductivity and permeability) must be reconstructed on a 3D volume using as input a 2D scanning. The inverse problem is furthermore very sensitive to measurement noise. Indeed, the direct problem attenuates significantly the high frequencies of the conductivity and the permeability. The problem must thus be regularized. This is done by adding some constraints on the considered targets. Those constraints represent a-priori knowledge or hypothesis on the target. One could for example make the hypothesis that the target is a single homogeneous sphere. The inverse problem would then reduce to the estimation of the radius, permeability and conductivity of that sphere.

A large variety of constraints may be considered. The choice should be made in a way that makes those constraints, at least approximately, satisfied by the target of interest; in our case, typical metallic parts encountered on a minefield. As our goal is to develop a system that is able to run on an embedded computer in real time, we also considered complexity of the possible models.

It should be noted that the complexity of the problem is highly increased by the fact that a standard metal detector is used, and therefore the emitting coil is moved together with the receiving coil (for the detector we use, a single coil is used). This implies indeed that the path and intensity of the eddy currents induced in the target vary from one measurement to the other.

In this section six simplified target models will be developed. For those models, the inversion procedure has a moderated complexity and no problem is expected for real time processing. Although simple, those models are expected to

be appropriate for a large variety of targets of interest. Some theoretical justifications are provided in this section and these are also supported by the experimental results presented in section 5.

For those simple target models we will not be able to recover the electromagnetic characteristics of the targets but only a derived characteristic that we call the target function. For each case, the meaning of the target function will be discussed. We will show that even if it is not uniquely linked to the local electromagnetic properties of the target, it contains valuable information on the shape and electromagnetic properties of the target.

2 Single small target

If the target is small enough, the incident magnetic field becomes homogeneous on the target volume. The corresponding vector potential is then

$$\vec{A}_{c0}(\vec{r}) = \frac{\vec{B}_{c0}(\vec{r}_t) \times \vec{r}}{2} \tag{8}$$

where $\vec{r}_t$ is the gravity center of the target. The corresponding voltage induced in the metal detector is:

$$V_c(s) = \frac{s}{2} \int_{V_t} \vec{J}_{t\,arget}(\vec{R}_t,s).(\vec{B}_{c0}(\vec{r}_t) \times \vec{R}_t)dV_t = s\vec{B}_{c0}(\vec{r}_t).\vec{m}_t(s) \tag{9}$$

where

$$\vec{m}_t(s) = \frac{1}{2} \int_{V_t} (\vec{R}_t \times \vec{J}_{t\,arget}(\vec{R}_t,s))dV_t \tag{10}$$

is the magnetic dipole moment of the target [7].

For linear materials in an homogeneous magnetic field, the magnetic moment must be a linear function of the magnetic field:

$$\vec{m}_t(s) = \vec{\vec{M}}_t(s).\vec{H}_c(\vec{r}_t,s) \tag{11}$$

where $\vec{\vec{M}}_t(s)$ is the magnetic polarizability of the target; by reciprocity [1], this is a 3 by 3 symmetric tensor:

$$\vec{\vec{M}}_t(s) = \begin{pmatrix} M_{xx}(s) & M_{xy}(s) & M_{xz}(s) \\ M_{xy}(s) & M_{yy}(s) & M_{xz}(s) \\ M_{xz}(s) & M_{xz}(s) & M_{zz}(s) \end{pmatrix} \tag{12}$$

The magnetic polarizability tensor encompasses the specific electrical and geometrical features of the target. It is frequency dependent. Fingerprint analysis for target classification can benefit from its properties. Some typical magnetic polarizability tensor are reported in [1 chapter 8].

Finally, the voltage induced across coil by the back-scattered field is:

$$V_c(s) = s\mu\vec{H}_{c0}^T(\vec{r}_t)\vec{\vec{M}}_t\vec{H}_{c0}(\vec{r}_t)I_c(s) \tag{13}$$

This last equation was obtained for a coil located at the origin in a horizontal plane. If the coil is translated to $\vec{r}_c$, the above equation becomes:

$$V_c(\vec{r}_c,s) = s\mu\vec{H}_{c0}^T(\vec{r}_t - \vec{r}_c)\vec{\vec{M}}_t\vec{H}_{c0}(\vec{r}_t - \vec{r}_c)I_c(s) \tag{14}$$

Strictly speaking equation (14) is only valid for a punctual target such as a dipole. For all other targets, the field is not homogeneous on the target volume and a model noise is introduced by assuming that the field is homogeneous. To analyze the effect of that modeling noise, the other source of noise must also be taken into account. We rewrite 14 as

$$V_c(\vec{r}_c,s) = s\mu\vec{H}_{c0}^T(\vec{r}_t - \vec{r}_c)\vec{\vec{M}}_t\vec{H}_{c0}(\vec{r}_t - \vec{r}_c)I_c(s) + \eta \tag{15}$$

where η is the total noise. The various sources of noise are discussed in section 1.

The total noise will limit the reachable resolution (see section 4). As long as the target modeling noise is small when compared to the other sources of noise, the homogeneity hypothesis is valid and does not decrease the reachable resolution. This will be the case if $r_{max} < f(d)$ where r_{max} is the maximal radius of the target and d is the best resolution that may reached in absence of target modeling noise (for a dipole target). Clearly, if a target is larger than the resolution, the hypothesis may not hold and one must either accept a lower resolution or user more adequate model. Some alternative models are proposed in the next sections. The precise upper bound for the target size is target dependent. Further research should allow the definition of this upper bound more precisely for a number of typical targets. This could be done by means of measurement or simulation.

Introducing the evaluation function of the detector (7) in (14), the output signal becomes:

$$V_m(\vec{r}_c) = \vec{B}_{c0}^T(\vec{r}_t - \vec{r}_c)\ddot{\Gamma}_t \vec{B}_{c0}(\vec{r}_t - \vec{r}_c) \tag{16}$$

The tensor

$$\ddot{\Gamma}_t = O\left\{\frac{sI_c(s)}{\mu}\ddot{M}_t(s)\right\} = \begin{pmatrix} \Gamma_{xx} & \Gamma_{xy} & \Gamma_{xz} \\ \Gamma_{xy} & \Gamma_{yy} & \Gamma_{xz} \\ \Gamma_{xz} & \Gamma_{xz} & \Gamma_{zz} \end{pmatrix} \tag{17}$$

is called the evaluated (by the detector) magnetic polarizability tensor. It reflects the target's characteristics measured by the detector. Its eigenvectors indicate the orientation of the target. The eigenvalues are invariant for a given target; they could thus be used as input of a classifier. Care should however be taken because different targets could have the same eigenvalues. Furthermore, the eigenvalues could be different for different exemplars of a given target and they could also change with the age of the target (typically, the oxidation of a metal strap could significantly change its resistance – at the limit, the strap could break, leading to an open circuit instead of a closed one), or with its environment (temperature, etc.).

Equation (16) is a non linear equation in the 9 unknowns ($x_t, y_t, z_t, \Gamma_{xx}, \Gamma_{xy}, \Gamma_{xz}, \Gamma_{yz}, \Gamma_{zz}$) Therefore, if the metal detector is used to sense the target answer in 9 well chosen positions, the 3D position of the target as well as its characteristic matrix A could be recovered by solving a non linear system of equations. To decrease the noise sensitivity, more points should be used and an error criteria should be minimized. The eigenvalues of the matrix are invariant for a given target and the eigenvectors provide information on the orientation of the target. This approach is currently under investigation. The main open questions are: how many measurement points should be used, what is the optimal scanning path and how to choose the initial values to ensure convergence to a valid solution? The possibility to recover the time dependent magnetic polarizability tensor ($\ddot{M}(s)$) is also considered. This could allow for a better target discrimination thanks to fingerprint analysis but, as explained above, this is not possible with a standard metal detector that does not provide access to the time decay of the coil voltage. Simple adaptations of the metal detector that could solve the problem are under investigation.

3 Two small targets

The case of two small targets in the field of the detector is now investigated. The objective is to point out the effect of the interaction of the targets on the measured EMF. The result developed here will be helpful for the analysis of other target arrangements (see next section).

It should be noted that even if the targets are small enough to be considered as dipoles from the detector's point of view, they may interact and it is in general necessary to take into account the exact shapes of the two targets to compute the coupling. Only if the two targets are sufficiently far from each other, the dipole approximation may be used to compute the coupling.

Two targets, located in $\vec{r}_1$ and $\vec{r}_2$, are excited by both the coil's incident field and by the field induced by the other target. If the dipole approximation is valid:

$$\begin{aligned} \vec{m}_1 &= \ddot{M}_1(\vec{H}_1^{inc} + \vec{H}_1^{sc2}) \\ \vec{m}_2 &= \ddot{M}_2(\vec{H}_2^{inc} + \vec{H}_2^{sc1}) \end{aligned} \tag{18}$$

where $\vec{H}_i^{inc}$ is the incident field of the MD on target i and $\vec{H}_i^{scj}$ is the scattered field from target j on target i. The field scattered by each dipole is:

$$\vec{H}_2^{sc1} = \frac{1}{4\pi\|\vec{r}_1 - \vec{r}_2\|^3}\left(\ddot{1}_{\vec{r}_1-\vec{r}_2}\ddot{1}_{\vec{r}_1-\vec{r}_2} - \ddot{I}\right)\vec{m}_1 = \ddot{C}_{21}\vec{m}_1$$

$$\vec{H}_1^{sc2} = \frac{1}{4\pi\|\vec{r}_2 - \vec{r}_1\|^3}\left(\ddot{1}_{\vec{r}_2-\vec{r}_1}\ddot{1}_{\vec{r}_2-\vec{r}_1} - \ddot{I}\right)\vec{m}_2 = \ddot{C}_{12}\vec{m}_2 \tag{19}$$

As $\ddot{C}_{21} = \ddot{C}_{12}$, let's note $\ddot{C}$ this tensor. Combining (18) and (19) leads to:

$$\vec{m}_1 = \left[\ddot{1} - \ddot{M}_1\ddot{C}\ddot{M}_2\ddot{C}\right]^{-1}\ddot{M}_1\left(\vec{H}_1^{inc} + \ddot{C}\ddot{M}_2\vec{H}_2^{inc}\right) \tag{20}$$

The expression of $\vec{m}_2$ is obtained by swapping indexes 1 and 2.

It appears clearly from (20) that the coupling induces two additional terms ($\ddot{M}_1\ddot{C}\ddot{M}_2\ddot{C}$ and $\ddot{C}\ddot{M}_2\vec{H}_2^{inc}$). For first order spherical targets, the polarizability matrix is diagonal $\ddot{M}_i = K_i s/[1 + sT_i]\ddot{1}$. Furthermore, if the two targets are

identical, the first additional term is the square of the second one. Both terms increase with the frequency and decreases with the distance.

For the first-order targets considered, the coupling increases with the frequency and becomes constant for frequencies higher than the cut-off frequency of the targets ($\nu > T_1 = T_2$) where it reaches a plateau. If higher frequency poles are excited, the coupling will decrease for frequencies higher than the pole characteristic frequency.

$\ddot{C}$ decreases asymptotically as r^{-3}. Therefore, at a given frequency, the first additional term decreases as r^{-6} and the second one as r^{-3}. For frequencies on the plateau, this gives respectively: $K_1 K_2 / (T_1 T_2) r^{-6}$ and $K_2 / T_2\, r^{-3}$

To summarize, if the distance is increased, or the frequency decreased, the coupling will decrease:

- For strong coupling, equation (20) should be used

- The first term ($\vec{M}_1 \ddot{C} \vec{M}_2 \ddot{C}$) will first vanish. Equation 20 then becomes:

$$\vec{m}_1 = \vec{M}_1 \left(\vec{H}_1^{inc} + \ddot{C} \vec{M}_2 \vec{H}_2^{inc} \right) \tag{21}$$

This is the case of weak coupling.

- Finally, the coupling completely vanishes, Equation (20) becomes:

$$\vec{m}_1 = \vec{M}_1 \vec{H}_1^{inc} \tag{22}$$

and the voltage sensed by the coil is:

$$V_m(\vec{r}_c) = \vec{B}_{c0}^T (\vec{r}_{t1} - \vec{r}_c) \ddot{\Gamma}_{t1} \vec{B}_{c0} (\vec{r}_{t1} - \vec{r}_c) + \vec{B}_{c0}^T (\vec{r}_{t2} - \vec{r}_c) \ddot{\Gamma}_{t2} \vec{B}_{c0} (\vec{r}_{t2} - \vec{r}_c) \tag{23}$$

As for a single target, if a number of measurements made in well-chosen positions are available, it should be possible to recover the targets position and the evaluated magnetic polarizability tensors by means of a non linear optimization. The number of unknowns is however significantly increased and more measurements are needed. If the coupling may be neglected, the number of unknowns is multiplied by two. If the coupling must be considered, 36 additional unknowns $O(\vec{M}_1^{ij}(s)\vec{M}_2^{kl}(s)) = C_{ijkl} \neq \vec{A}_1^{ij} \vec{A}_2^{kl}$ appear.

We are currently investigating this approach. The same questions as for the single target case must be answered. More problems are however expected because the choice of initial values becomes more complex and the resolution time increases.

4   Discrete number of small targets

In case of strong coupling, the results derived for two targets may not be generalized. For weak coupling, the generalization of (21) gives:

$$\vec{m}_i = \vec{M}_i \left(\vec{H}_i^{inc} + \sum_{j \neq i} \ddot{C} \vec{M}_j \vec{H}_j^{inc} \right) \tag{24}$$

If the coupling can completely be neglected, the above equation becomes:

$$\vec{m}_i = \vec{M}_i \vec{H}_i^{inc} \tag{25}$$

An the detector output becomes:

$$V_m(\vec{r}_c) = \sum_i \vec{B}_{c0}^T (\vec{r}_{ti} - \vec{r}_c) \ddot{\Gamma}_{ti} \vec{B}_{c0} (\vec{r}_{ti} - \vec{r}_c) \tag{26}$$

The positions of the dipoles, their characteristic matrices and the couplings could theoretically be recovered by means of a non-linear optimization as already discussed in the case of a single or two targets. An additional problem is to determine the suitable number of targets. There is furthermore a fast increase of the number of unknowns with the number of targets. The increase is less dramatic in absence of coupling; but still the number of targets should remain limited to keep a tractable problem. The maximum number of targets for which the system may be solved is currently under investigation.

5   Distribution of independent dipoles

For a planar distribution of dipoles at a given depth, equation (26) becomes:

$$V_m(\vec{r}_c) = \int_{S_t} \vec{B}_{c0} (\vec{R}_t - \vec{r}_c) \ddot{\Gamma}_t (\vec{R}_t) \vec{B}_{c0}^i (\vec{R}_t - \vec{r}_c) dS_t \tag{27}$$

which may be expended as follows:

$$V_m(\vec{r}_c) = B_x^2 * \Gamma_{xx} + B_y^2 * \Gamma_{yy} + B_z^2 * \Gamma_{zz} + 2B_xB_y * \Gamma_{xy} + 2B_xB_z * \Gamma_{xz} + 2B_yB_z * \Gamma_{yz} \qquad (28)$$

Equation (28) is a sum of 2D convolutions that cannot be inverted. This problem can only be solved for specific targets for which the magnetic polarizability tensor may be simplified. Among others, here are two such cases:

- For a spherical homogeneous target, the magnetic polarizability tensor is diagonal and its three elements are equal ($\Gamma_{xx} = \Gamma_{yy} = \Gamma_{zz} = T$). Then, the measured voltage is:

$$V_m(\vec{r}_c) = \left\| \vec{B}_{c0} \right\|^2 * T \qquad (29)$$

- For a horizontal loop the only non-null term of the magnetic polarizability tensor is $\Gamma_{zz} = T$. Then, the measured voltage is:

$$V_m(\vec{r}_c) = B_{c0}^z{}^2 * T \qquad (30)$$

For these two cases, the target function may be recovered by means of a deconvolution process using a suitable kernel. This kernel depends on the distribution of the incident induction field $\vec{B}_{c0}(\vec{r})$ and of the depth of the target distribution.

One might think that a 3D deconvolution process could be used to recover a 3D distribution of targets from a 3D scanning. Obviously such a 3D scanning would be difficult to perform in practice because a very long time would be needed to perform the scanning. Furthermore, there is a more fundamental reason that prevents such a 3D reconstruction. Indeed, the input of the reconstruction should be the MD output on a 3D lattice spanning the complete space where the measurement is significant. This includes measurement over and below the buried objects which is obviously impossible. One may even show that once the measurement of the magnetic field is known on one plane above the soil, it may be computed on any other plane above the soil. This is due to the fact that in absence of currents, the magnetic field may be expressed as the gradient of a scalar potential:

$$\vec{B} = -grad(V^*) \qquad (31)$$

The solution of such an equation is uniquely determined by the knowledge of the boundary conditions. It is sufficient to know the potential on the boundary (Dirichlet problem) or its normal derivative (Neumann problem)[7]. Therefore, once the vertical component of the magnetic field (normal derivative of the potential) is known on a plane above the soil, the magnetic field may be computed in all the half-space above that plane.

The above reasoning is based on the assumption that the magnetic field is sensed simultaneously on the whole scanning plane or equivalently that the current density in the target does not change from one measurement to the other. This would be the case if the emitting coil remains fixed and only the receiving coil is moved to perform the scanning. By reciprocity, a fixed receiving and a moving emitting coil would be equivalent. With a standard metal detector, the emitting and receiving coils (which are in some case the same physical coil) are rigidly fixed and move together. Therefore, the constant excitation hypothesis is not valid. However, for the target models that lead to a convolution (sphere and loop), equations (29) and (30) show that the configuration is equivalent to a fictive fixed emitting and moving receiving coil. As an example, for spherical target, the equivalent fixed emitting coil would generate a file of constant modulus on the region of interest and the receiving coil would generate a field whose module is the square of the module of the field generated by the real coil (see equation (30)).

By analogy to axial stereovision, one might think that it could be possible to recover the depth of the targets if the scanning is performed on two planes at different height. The above discussion shows however that this is impossible. For any hypothesized depth, a possible dipole distribution will be found. Without a priori knowledge on the distribution, it is impossible to find out the real dipole distribution and thus the real depth. Indeed, each distribution found will accurately predict any measurement that could be made in the accessible half space. We are however investigating techniques similar to the focusing of a camera to find the depth of the target. The image will look blurred or present artifacts if the depth used is not the right one. The depth will then be chosen to get the 'best' restored image. For an automatic depth estimation, a criteria rating the quality (no blurring, no artifacts) of an image must be defined. An alternative is to present the result at different depth to the user that will then use his own criteria to select the best image. The system will then return the corresponding depth.

As discussed above, the scanning at different heights is useless. However, scanning with different orientations of the incident field may bring more information on the target. This could amongst other allow for assessing all elements of the magnetic polarizability tensor. This could be done using a synchronized network of coils. An appropriate coils geometry and excitation, will allow for generating an incident magnetic field for which only one component (B_x, B_y or B_z) is non-null in a defined region of the space. If similarly, an appropriate combination of the voltage sensed by the

receiving coils is used, it will be possible to recover independently each component of the evaluated magnetic polarizability (17).

In section 4, a general model suited for a discrete number of small targets has been developed. With that model, the inversion is performed by a non-linear optimization. If the targets are at constant depth, if the coupling can be neglected and if the magnetic polarizability is spherical or loop like, the inversion is simplified and becomes a deconvolution. Indeed, the problem may then be seen as a particular case of the dipole distribution and equations (29) or (30) yields. The target function becomes a sum of Dirac functions. A Dirac function appears at each target location and its amplitude characterizes the corresponding target.

6   Elongate targets and disks

The field emitted by a planar disk or a planar elongated target may be modeled by a distribution of dipoles (see Figure 2). To use (29) or (30), we have to show that the corresponding dipoles are independent and that they are equivalent to small spheres or loops.

This is in general not the case. Typically, for a closed loop, the equivalent dipoles must be coupled by any mean to produce the same current in each dipole as the one flowing through the original circuit. This strong coupling (even if it is not a mutual coupling by magnetic induction) violates the hypothesis of dipole independence. Therefore, (30) may not be used to model an extended planar loop and the model developed in the next section should be used instead (equation (36)).
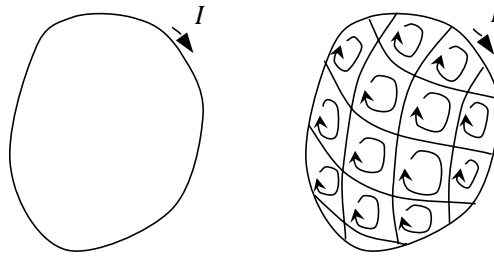

Figure 2 - The equivalence of a current loop carying a current I and a current mesh. A current flowing in inner mesh is cancelled by currents flowing in surrounding meshes. The overall remaining current mesh is the original bordering loop.

To be modeled accurately by a distribution of independent dipoles, the current density induced in the target by a punctual excitation (a focalized magnetic field for instance) should remain localized inside a sphere of radius d (see section 2). The current outside that sphere may be neglected if the magnetic field generated by those currents may be neglected. In first approximation, this is equivalent to require a negligible dipolar moment. Typically, for circular currents, $\int_{d}^{\infty} J_{\theta}(r).r^2 dr$ must be negligible. Therefore, the current should decrease faster than r^{-2}.

To use equation (30) the spherical symmetry must furthermore be valid.

To quantify the model limits, numerical simulations or experimental results should be performed. The experimental results presented in section 5 shows that the model is valid for the test targets considered. Numerical simulations are currently under investigation. The following discussion presents a qualitative discussion on the model limits for a flat disk.

At low frequencies, the disk cannot be modeled by independent dipoles because the field generated by the target is negligible in comparison to the excitation field. The current then decreases as r^{-1} (same EMF for each circle and resistance linear in r) and the magnetic moment increase as r. In other words, the external part of the disk emits the major part of the magnetic field.

For higher frequencies, the field generated by the disk increases. Larger current loops encompasses the excitation field as well as the field generated by the inner current loops which partially compensates the excitation magnetic field. Therefore, the current density decreases faster and the independent dipole model becomes valid. This phenomenon is linked to the skin effect.

A standard metal detector, generates low as well as high frequencies. The lower frequencies will be responsible for a model error. This effect is however limited by the fact that the voltage induced in the detector coil is proportional to the derivative of the current in the target. Therefore, higher frequencies have more influence on the detector output.

7   Single extended closed winding

For a single large closed loop, lying on a horizontal plane at a given depth,

$$V_c(\vec{r}_c, s) = s^2 \frac{I_c(s)}{Z_t(s)} K^2(\vec{r}_c) \tag{32}$$

In this expression, $Z_t(s) = r_t + sL_t$ is the impedance of the loop and $K(r_c)$ is the mutual coupling between the detector (located at $\vec{r}_c$) and the target which may be expressed as follows:

$$K(\vec{r}_c) = \iint_{S_t} \vec{B}_{c0}(\vec{R}_t - \vec{r}_c).d\vec{S}_t = \iint_{t\arg et-plane} B_{c0}^z(\vec{R}_t - \vec{r}_c).N(\vec{R}_t).dS_t \tag{33}$$

where S is the Region inside the target and $N(\vec{R}_t)$ is defined as follows:

- 1: inside the target area S,

- 0: outside the target area.

Equation (33) shows that the coupling may be expressed as a 2D convolution: $K = T * B_z$. The output of the metal detector is:

$$V_m = O\{V_c(s)\} = O\left\{\frac{s^2 I_c(s)}{Z_t(s)}\right\} K^2 = \alpha K^2 \tag{34}$$

where

$$\alpha = O\left\{\frac{s^2 I_d(s)}{Z_t(s)}\right\} \tag{35}$$

Hence:

$$Y = \pm\sqrt{|V_m|} = \frac{N}{\sqrt{|\alpha|}} * B_z = T * B_z \tag{36}$$

To compute Y knowing V_m, the sign ambiguity must be resolved. This may be done by using a heuristic algorithm that uses the fact that a null mutual is seldom at locations where no sign change occurs. The target function T is proportional to N which has been defined above and may be recovered by means of a deconvolution process. The definition of the target function shows that there is a clear link between that function and the loop shape.

The above derivation may be generalized to a large planar closed winding. The value of N function at a given point may then be interpreted as the number of turns of the winding around that point.

Equation (36) may not be generalized to more than one target. Indeed, for two targets the equation becomes:

$$Y = \pm\sqrt{|V_{m1}|} \pm \sqrt{|V_{m2}|} = T_1\,'*B_z + T_2\,'*B_z = T\,'*B_z \tag{37}$$

One sees that Y may not be computed using the only available measurement $|V_m|$. Apart from the sign ambiguity, the problem comes from the fact that $\sqrt{|V_m|} \neq \sqrt{|V_{m1}|} + \sqrt{|V_{m2}|}\big|_z$ except if in any point only one of the targets induces a significant voltage in the detector coil. This will be the case if the distance between the targets is large enough to observe well separated peaks in the raw image.

Equation (36) may however be used for several close targets if it is possible to first separate their contribution. We are currently investigating the possibility to separate the contribution of each target by means of pole estimation of the time-domain impulse response. This is however not possible with a standard metal detector that uses an evaluation function (5) to compute a single value from the target impulse response. The impulse response is thus not available for data processing. The feasibility to enhance the metal detector to be able to get the impulse response in investigated.

8   Conclusion

In the previous sections, six target models have been developed. They may be used to represent a large variety of real targets as mine firing pins or metal straps, barbed wires, etc.

We have mentioned the possibility to recover the position and the evaluated magnetic polarizability tensor of a discrete number of targets through a non-linear optimization process.

We have also shown that for a number of target models (section 5, 6 and 7), the imaging process may be modeled by a convolution filter. The restoration technique presented in section 4 will then be used to image the target.

Depending on the model, different imaging kernels, different raw image input and different target function interpretation must be used. The results are summarized as follows:

Target type	Raw image	Kernel	Target function
Distribution of independent spherical dipoles	$V_m(x, y)$	$\left\|\vec{B}_{c0}\right\|^2$	$T(x, y) = \Gamma_{xx}(x, y) = \Gamma_{yy}(x, y) = \Gamma_{zz}(x, y)$
Distribution of independent horizontal loop like dipoles	$V_m(x, y)$	$B_{c0}^{z\,2}$	$T(x, y) = \Gamma_{zz}(x, y)$
Single planar extended closed winding	$\pm\sqrt{V_m(x, y)}$	B_{c0}^{z}	$T(x, y) = \dfrac{N(x, y)}{\sqrt{\alpha}}$ where $N(x,y)$ is the number of turns of the winding around the point (x,y) and $\alpha = O\left\{\dfrac{s^2 I_d(s)}{Z_t(s)}\right\}$ reflects the electrical characteristic of the winding.

Table 1 : imaging convolution characteristic for various target models

The various kernels may be computed once the depth of the target and the field generated by the metal detector for a unit current ($\vec{B}_{c0}$) is known. We have shown that scanning at various heights is useless to estimate the depth of the target. The depth could however be provided by another sensor or selected to provide the 'best' image (kind of focusing).

For the planar winding, no questionable hypothesis were made; for a discrete number of small spherical or loop like target, the only open question is the maximal allowable size for the target. For the elongated or disk targets however, a number of hypothesis that could fail for some real targets where made. Numerical simulation should be performed to assess more precisely the limits of this model. Experimental results presented in section 5 are however promising.

4 IMAGE RESTORATION

1 Problem statement

We have shown in section 3 that the imaging process may be modeled for a number of targets of interest by a convolution process:

$$g(x, y) = T(x, y) * h(x, y) + \eta(x, y) \tag{38}$$

where $g(x, y)$ is the raw image built from the metal detector output by an appropriate scanning, $T(x, y)$ is the target function, $h(x, y)$ is the imaging kernel and $\eta(x, y)$ is the noise.

Table 1 summarizes the raw image, the target function and the imaging kernel to use for the various target models for which equation (38) may be used.

Various sources of noise have to be considered such as:

- use of an erroneous target model

- use of an estimation of the magnetic field generated by the coil $\vec{H}_{c0}$. Estimation errors are due to an erroneous modeling of the geometry of the coil but also to an error on the coil position and orientation

- electronic and quantification noise.

- Effect of the soil. The presence of the soil has not been taken into account in the modeling. This is justified if the soil is not conductive and not magnetic. A magnetic soil will disturb the magnetic field generated by the coil and back scattered by the target; the shape of the imaging kernel will change. Furthermore, non-linearities could appear. The effect of a conductive soil is twofold. First, it back-scatters energy and will therefore be at the origin of clutter. Second, the field illuminating the target is the sum of the field generated by the coil and by the soil. Hence, the imaging kernel will be distorted. This distortion will however remain limited because the target depth is in general much smaller than the skin depth of soils at the frequencies used.

As a typical example, Figure 3 shows the kernel for the spherical dipole distribution at various depth. Figure 4 presents the corresponding Fourrier transform. These figures show that the imaging process is a low pass filter and that the restoration process will have to amplify significantly the high frequencies. Therefore, care should be taken to avoid a strong amplification of the noise.

The reachable resolution is function of the signal to noise ratio and the shape of the imaging kernel. The reachable resolution will decrease when the signal to noise ratio or the cut-off frequency of the imaging kernel is reduced. The noise is function of the target depth and detector height above the ground. Indeed, the electronic noise is independent of

the target depth or detector height, but the other source of noises such as the coil modeling error may vary. The signal decreases very fast with the depth. Furthermore, the imaging kernel becomes a stronger low pass filter when the depth is increased. Therefore, the reachable resolution decreases fast when the distance between the target and the detector is increased.

2   Restoration filter

It has been shown [11] that image deconvolution is an ill-posed, meaning that the solution of the problem does not always exist, and in case it exists it is not unique and highly sensible on the input data. The problem can however be regularized and many methods have been developed (see[10] for a review) to this end.
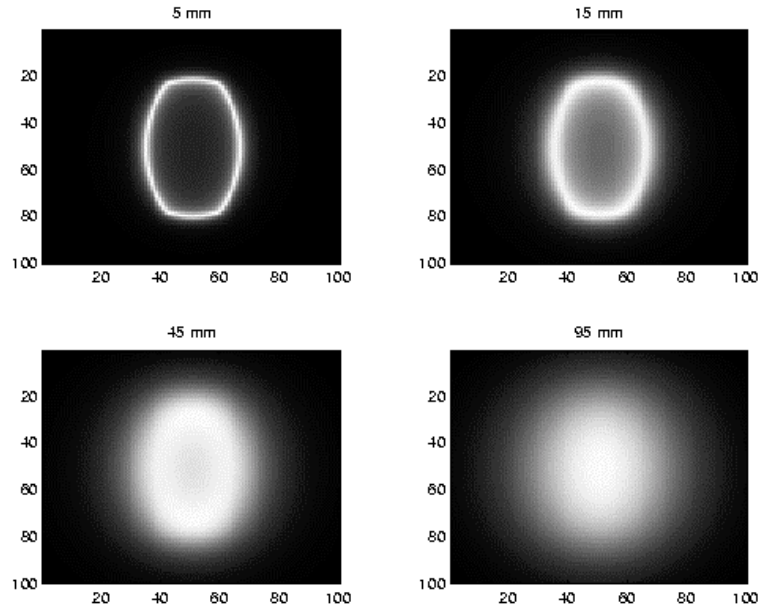
Figure 3 – Samples of kernels taken along a plane parallel to the detector coil's plane and at heights of 5, 15, 40 and 95 mm (from left to right and top to bottom). These four views do not share the same colormap. Maximum values at 5 mm are obviously much higher than the one at 95 mm.
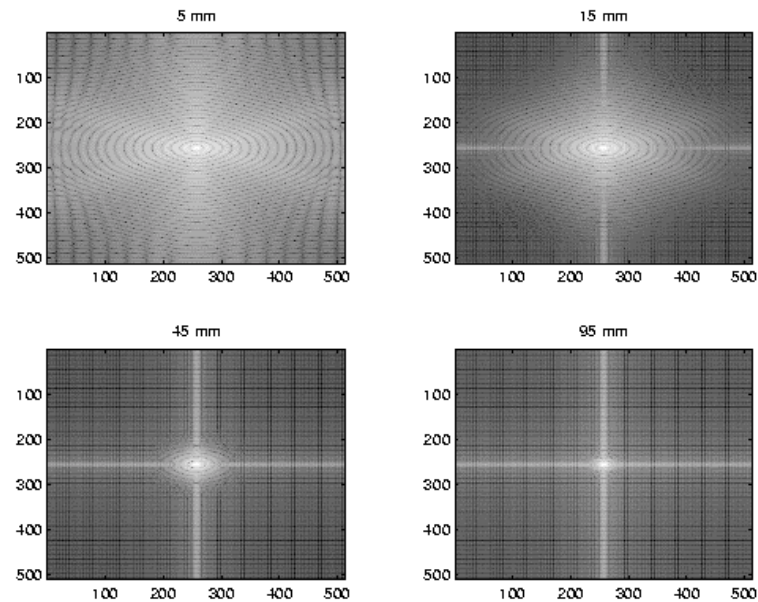

Figure 4 – Corresponding PSF of previous kernels. The null frequencies are centered. The log of the PSF is displayed (for a better visualization) and the images do not share the same colormap.

A widely used approach is the Wiener-restoration [9]. This minimizes the mean square error between the estimate and the true image using a linear operator under the assumption of signal-independent noise, a linear degradation, the stationnarity of the images and degradation filter and a circulant approximation. The following Fourier-domain expression is then obtained for the restoration filter:

$$M(u,v) = \frac{H^*(u,v)}{|H(u,v)|^2 + \dfrac{S_{nn}(u,v)}{S_{ff}(u,v)}} \tag{39}$$

where $S_{nn}(u,v)$ and $S_{ff}(u,v)$ are the spectral densities of the noise and of the target function. In the absence of noise ($S_{nn} = 0$), the Wiener filter reduces to the ideal inverse filter.

The restored image may then be computed:

$$\hat{T}(u,v) = M(u,v)G(u,v) \tag{40}$$

This approach is not optimal for our problem because many underlying hypotheses are not valid. Typically, the modeling noise (that could well be the principal source of noise) is correlated with the ideal image. This noise is furthermore difficult to estimate. Ideally, S_{ff} should be computed on a database of representative target functions. It is difficult and expensive to gather such a database. Better results could even be obtained using a heuristic estimate of S_{ff} based on the blurred image. One then implicitly gets a restored image that is a non-linear function of the blurred image. This shows that the fact that the method restricts the restored image to a linear function of the blurred one is a severe drawback.

The method is however easy to implement and experimental results show that good results are obtained. We are currently investigating more sophisticated methods because they could provide sharper images but the main goal is to avoid the manual parameter tuning.

3 Practical considerations

The restoration filter was computed using equation 39. S_{nn} was chosen constant ($S_{nn} = \sigma^2$) and for S_{ff} an heuristic estimate of the spectral density of the target function was used. The target function was supposed to be a gaussian of adjustable variance and amplitude. A 4-pixels variance was chosen for all the experiments. The amplitude of the gaussian (A) may be computed using the DC component of the inverse filter.

$$A = \langle T(x,y) \rangle = \frac{\langle g(x,y) \rangle}{\langle h(x,y) \rangle} \tag{41}$$

This leads to the following S_{nn}/S_{ff} ratio:

$$\frac{S_{nn}}{S_{ff}} = \frac{\sigma^2}{S \dfrac{\langle g(x,y) \rangle}{\langle h(x,y) \rangle}} \tag{42}$$

where S is a spectral density of the gaussian with the selected variance and unit amplitude. σ is manually adjusted to get good results.

In practice, the target function is not a gaussian and better results were obtained using:

$$\frac{\hat{S}_{nn}}{S_{ff}} = \frac{\sigma^2}{S \dfrac{\max(g(x,y))}{\langle h(x,y) \rangle}} \tag{43}$$

The advantage of the method is that σ does not vary in a wide range. Hence it may easily be tuned with a few iterations.

5 EXPERIMENTAL RESULTS

In this section, the experimental setup will first be presented. Results will then be shown for targets that can be modeled by an independent dipole distribution and by a closed winding. A discussion on the field depth and on the importance to select the appropriate model will then be presented. Finally, some conclusion will be drawn.

1   Experimental setup

The experimental setup is presented in Figure 5. The MD is towed by a mechanized X-Y table controlled by a PC. A square area of 40 x 40 cm is scanned with a 5mm step. The numerical output of the metal detector is recorded in each point to build a raw image of 81 by 81 pixels.

Figure 5: Picture of the lab facilities. The MD is towed by a mechanized X-Y table controlled by a PC.

As explained earlier, most soils do not influence significantly the detector output. This is the case with the soil we used and, to simplify the experiments, the targets where laid on the ground. To make it short, the distance between the target plane and the detector coil is called the target depth. In practice, the detector is scanned as close as possible to the soil and those two quantities are nearly equal.

2   Dipole distribution

To check the validity of the dipole distribution model (equations 29 and 30), a small sphere (to check equation 29) and a small loop (to check equation 30) have been used. As the results for the sphere and the loop are similar, only the results with the loop have been presented. More complex targets have then been tested. For those shapes, the spherical dipole distribution model (equations 29) has been used. In order to comply with the model, these targets must not include large current loops. Therefore, these targets are all made up of thin copper wire. Among them, we report here the case of a straight wire 10 cm long, a X like shape made up of two bent copper wires of overall dimension 8 x 12 cm and finally a flag like shape of overall dimension 8x16.

The used sphere is a 11 mm diameter steel ball. Figure 6 shows the raw image gathered for a ball buried 30 mm under the detector and the restored image together with the filter and error images (in the spatial domain). The noise factor is $\sigma = 5\,10^{-3}$. The pixel size is 0.5 cm. The restored image shows a focused disk of about 3 pixels diameter, which is close to the real ball diameter. The error image is computed taking the restored image as input of the blurring process. The error is then: $e = g - \hat{T} \otimes h$. The error image presents a ghost of the coil. This results from a misalignment of the detector head. Indeed the head support was slightly twisted around the vertical axis and the coil plane was likely a little tilted (planes of the coil and of the scan were not perfectly parallel). Anyway, the resulted image shows a good agreement with the original target size and shape.

Figure 7 shows the same ball buried at 5.5 cm ($\sigma = 5\,10^{-2}$) and 8 cm ($\sigma = 5\,10^{-1}$). As explained in section 1, the achievable resolution decreases with the distance of the target to the coil. Therefore, the restored shape spreads out and extend clearly the size of the ball. In order to assess the resolution achievable by of the used Wiener filter in absence of
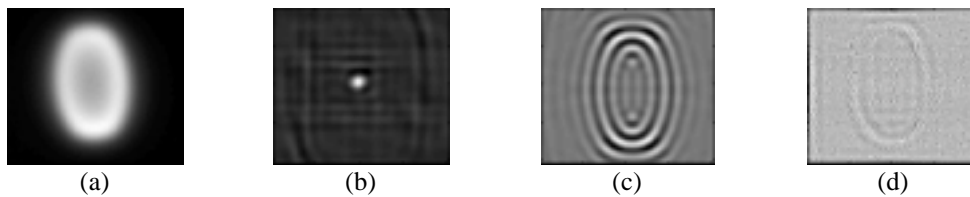

| (a) | (b) | (c) | (d) |

Figure 6 – Reconstruction of a steel ball at a depth of 3 cm. (a) original raw data. (b) restored image. (c) filter. (d) error.
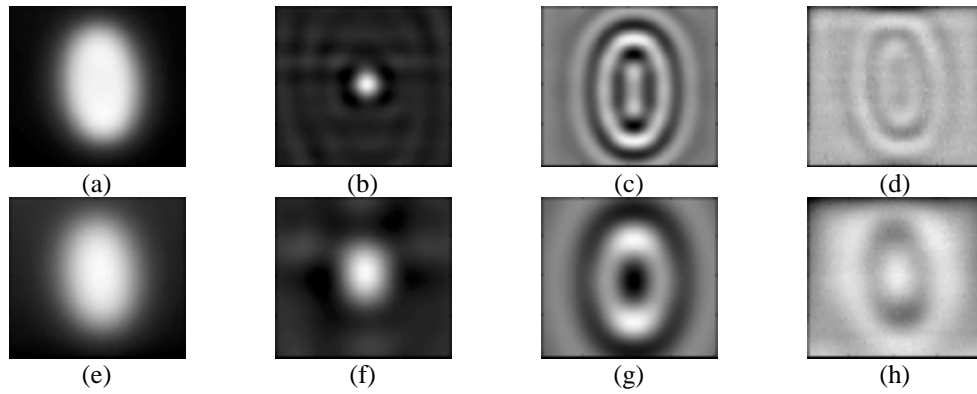
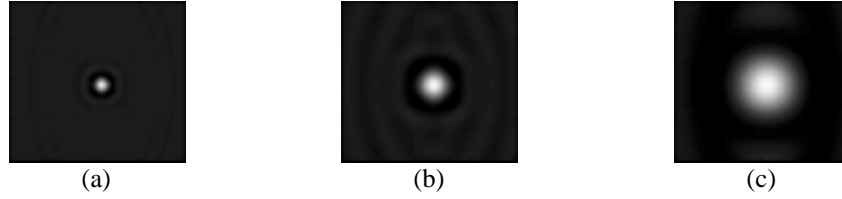Figure 7 – Reconstruction of the same steel ball at depth of 5.5 cm (a-d) and 80 cm (e-h).

Figure 8 – Assessment of the achievable resolution at the previous 3 depths (a: 3 cm, b: 5.5 cm, c:8 cm).

modeling error on the direct filter, Figure 8 shows the product of the direct and the Wiener filter: $H(u,v).M(u,v)$ transformed back in the spatial domain. The three views demonstrate that, the resolution can not be better than a few ten pixels as the depth goes beyond 5 cm.

Figure 9 to Figure 11 present respectively the results for a single straight wire an X and a flag like shape. All shape are made of copper wire of 3mm diameter. The straight wire is 10 cm long and 1 cm deep. The X like shape it has an overall dimension 8 x 12 cm and is 4 cm deep. Finally, the flag like shape has an overall dimension 8x 16 cm and is 4 cm deep.

The results are encouraging as in all cases, the shapes may be recognized. One may also notice that the dimensions of the imaged shapes are correct and that the corners are rather well recovered. As could be expected, the best results are obtained with the straight wire that is the closest to the coil (1cm).

For the straight wire a noise factor $\sigma = 10^{-2}$ was used. The choice of that value is not critical because the imaging filter has a high bandwidth due to the small depth and the inversion is rather easy. For deeper targets, the low pass character of the imaging filter become more pronounced and the selection of the right noise factor becomes more tricky. If the factor is too low, the filter amplifies too much the high frequencies and too much noise become apparent in the restored image. . On the opposite, if the factor is too high; the raw image is too little restored and the resulting image remains so blurred that the shape may not be recognized. In practice, only few trials where needed to find the right factor. The results presented where obtained with $\sigma = 1$.

Figure 9 – Result of a straight copper wire, 10 cm long, 1cm deep. The wire is tilted of 30º.
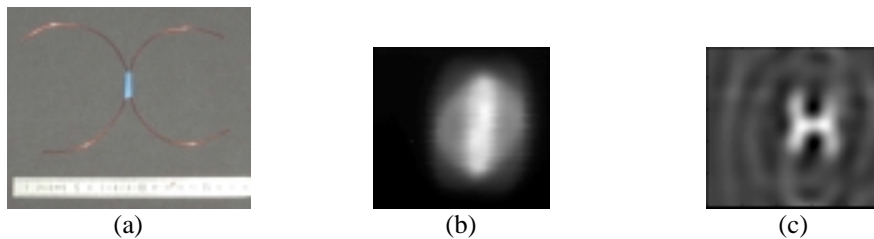
(a) raw image, (b) restored image.

Figure 10 – Result of a X like shape, made up of 2 bent copper wire (8x12cm, 4cm deep).

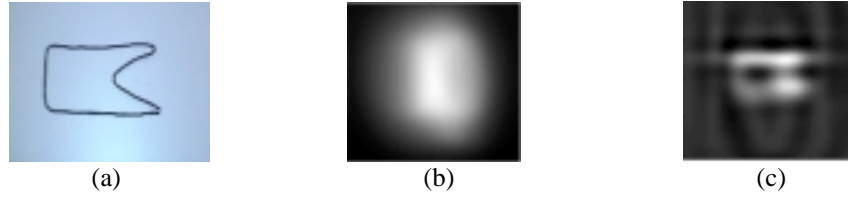(a) target picture (rotated of ¼ turn), (b) raw image and (c) restored one.

(a)   (b)   (c)

Figure 11 – Result of a flag like shape made of copper wire (8x16cm, 4cm deep).

(a) target picture (b) raw image and (c) restored one.

3   Closed winding

To check the validity of the closed winding model, (equations 36), a large rectangular loop of highly resistive wire has been built. It was mandatory to use highly resistive wire to avoid saturation of the metal detector. In practice, the selection of the wire resistance and the number of turns to use was critical. The answer of most tested targets presented either a saturated or a too weak answer. The problem is that we don't have any control on detector's gain. This is fine for detection of the target but to use the detector for imaging purpose, saturation must be avoided and the hardware should be adapted to allow the gain to be controlled.

The test rectangle is presented in Figure 12. It is build of two (serial) rectangular loops of resistive wire. Its size is 12x 8 cm and it is 8 cm deep. To understand the presented results, remember that the raw image is first be transformed using $Y(x, y) = \pm\sqrt{V_m(x, y)}$ and that the target function at a given point is proportional to the number of turns of the winding around that point. Ideally, for the test target, the restored image should present a constant value inside the rectangle and zero outside. The result obtained is in good concordance with the model. The shape may be recognized and the size is correct. The noise factor used was $\sigma = 0.5$.

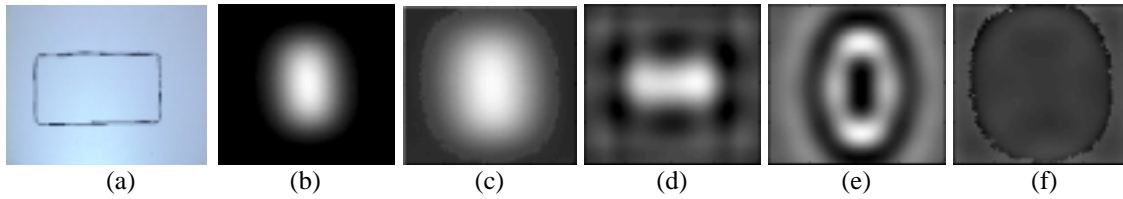(a)   (b)   (c)   (d)   (e)   (f)

Figure 12 – Restoration of a target made up of a rectangular loop of low conductive wire buried at 8 cm.

(a) target picture, (b) raw image, (b) corrected input (c) restored image, (d) filter in the spatial domain, (e) reconstruction error.

4   Kernel selection

To get an interpretable image of the buried target, the right kernel ($H(u, v)$) should be used. As explained in section 7, it is impossible to find the right model or the right depth using only the metal detector output. Indeed, for each hypothesis, a target shape will be found and the reconstruction error will not be bigger for a wrong model than for the good one. This is due to the fact that an infinite number of targets may back-scatter the filed sensed by the detector.

The only way to select the right target model is to use a priori knowledge on the expected targets. If the right target model is used, a sharp interpretable image will be obtained. In practice, the restoration may be performed with several target models and the user may then select the 'best' image. Typically, if a complex known shape is recovered, there is little chance that this was accidental and the right model was most probably used. If a criteria for a (good' image may be defined, this selection could also be automated. This approach is currently under investigation.

To determine the depth of the object, a similar approach could be used but the depth could also be provided by another sensor as a ground penetrating radar.

The problem of depth selection may be compared to the focusing of an optical system. There also, a-priori knowledge on a 'good' image is used to focus the system. If the field depth is large, the depth may not be recovered with a high accuracy. For our imaging problem, the same holds, but apart from the impossibility to recover the object depth, a large field depth has the advantage that a generic kernel computed at medium depth may be used for all depth of interest.

The results presented in Figure 13 show that this is not the case and that the right kernel should be selected. The consequence from that is that the depth of the object may be determined with a good accuracy.

For each view, the noise factor used is $\sigma = 0.5$. Images a-c result from the restoration of a ball 3cm deep using the kernel computed for 1 cm, 3cm and 9 cm. One sees that with a wrong depth, the resulting image is blurred and a ghost may even appear. Results are even worse for images e-f where a ball buried at 8 cm is restored using the kernel computed at 1, 3 and 8 cm.
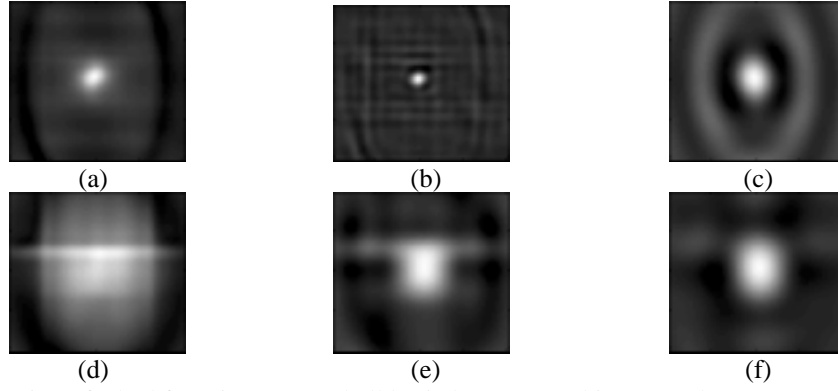
Figure 13 – Illustration of a bad focusing. (a-c) a ball buried at 3 cm and is restored at 1 cm (a), 3cm (b) and 9 cm (c). (d-f) a ball is buried at 8 cm is restored at 1 cm (d), 5 cm (e) and 8cm (f)

Finally, Figure 14 demonstrate that the right target model must be used. On that example, a brass loop of 30 mm diameter is imaged using the model of a spherical target (which was successfully used for the conductive ball or the open copper wires). Using that kernel, it is impossible to retrieve the real shape of the target whatever the noise factor is ($\sigma = 0.5$ for the presented result).
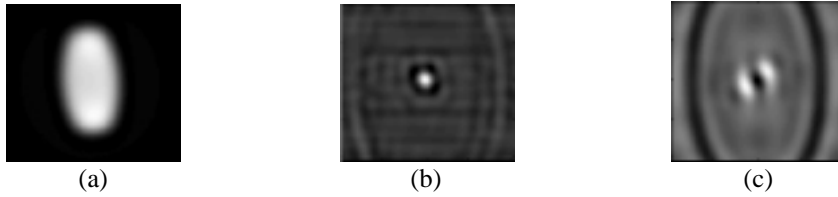

Figure 14 – Illustration of the restoration using a bad kernel. (a) raw image of a brass loop of 30 mm diameter buried at 3 cm restored using (b) the right kernel, (c) the kernel for a spherical target

5   Conclusion

Several experiments have been conducted to check the validity of the models developed in section 3. Good results were obtained. It was indeed possible to recover interpretable shape information. The quality of the restored image decreases with the target depth and good results were obtained up to about 10 cm. The exact depth limit is function of the size of the object of interest and better restoration techniques could increase the depth limit. The necessity and the way to chose the right kernel derived from the appropriate model and depth was discussed.

In section 4, a number of opened questions didn't receive a complete answer from a theoretical point of view. For instance: what is the maximal size for a target to be modeled by a single dipole? Is the independent spherical dipole distribution a good model for elongated targets? The experiments showed that a 1cm diameter sphere may accurately be modeled by a spherical dipole and that for all the elongated targets tested (straight wire, X, flag), the model is appropriate and allows a good shape recovery.

The restoration procedure is based on the deconvolution of the raw image using a Wiener filter. To compute the restoration filter, the direct imaging kernel must be known and the noise factor must be selected. The computation of the kernel was based on a numerical simulation of the magnetic field generated by the coil's head. The noise factor was selected by a trial and error procedure. Experiments showed that a good factor may be found with a limited number of trials. Investigations are conducted to adjust automatically this noise factor.

Experiments showed that the main noise is due to an error on the imaging kernel. This error does not come from an error on the simulated magnetic field but is rather due to an error on the coil position and orientation. To be more precise, the X-Y table provides a precise positioning of the sensor but the coil suffers from misplacement and misalignment. We are currently introducing some correcting parameters in order to take into account both the rotation of the coil around its axis and its tilt with respect to the horizontal plane.

6   CONCLUSION

This paper has paved the way for designing signal processing algorithms, and more especially imaging algorithms, relying on some basic but yet fundamentals physical principles of the magnetic induction technology.

We have started with a glance at the operation of the metal detector. It was shown that, with the frequency band used by the detector, the quasi-static magnetic regime may be used for the modeling. Then, a couple of basic target models have been passed in review, from the single small one, which reduces to a magnetic dipole to the more complex large closed loop. It has been shown that a priori knowledge is required to recover some parameters of interest such as the depth of the target or the model to use. Each model has been detailed and its validity bounds have been discussed.

Some experiments have been conducted to show the validity of the models developed. Both point-like and open wire objects have been imaged using an imaging algorithm tuned for uncoupled dipoles-like targets. The large closed loops winding, coplanar to the detector coil, has also been experimentally checked out. Both show a good agreement with the theoretical developments since well-focused images have been obtained with only a little need of hand-tuned parameters (the noise factor).

The exact limits of the developed models have still to be determined. It could well be that some targets of interest for the deminer lead to poor results because the models are not appropriate. Typically, for some targets, significant currents could be induced in large loops or anisotropic dipoles could be excited. The maximal depth to get usable results with the targets encountered on a real minefield must also be determined.

This work has triggered a wide amount of questions. To answer those questions, more simulation and trials should be performed. Some improvements are currently under investigation such as the possibility to use more complex restoration methods. The main objective is to avoid the manual tuning of the parameters. The filter should automatically adapt itself to the (local) content of the image. The possibility to automatically find the target depth is also considered.

The main objective of the research was to get as much information as possible on the targets with a classical metal detector. Promising results were obtained, but it appeared that some minor adaptation of the detector could lead to a much better system. Typically, a gain control should be provided to avoid saturation. The possibility to sample the voltage time decay would bring additional useful information (fingerprint analysis).

Many hypotheses on the target may be relaxed if a true bistatic sensor is used. Therefore, fewer models would be needed and better images could be expected. This kind of sensor should integrate two separated coils. For instance, a classical metal detector could be used as moving emitter. The receiver could be left at a specific location when the emitter is scanned over the field. It should be noticed that such a bistatic apparatus is well known in non-destructive testing applications. Therefore, a little effort should be required to adapt it to the case of demining.

Some advanced induction techniques are currently investigated. The objective is to recover all of the parameters of the magnetic polarizability tensor and their spectral characteristics (set of poles). A set of coils of same diameter with appropriate relative locations and excitation currents will allow for controlling the orientation of the incident magnetic field along a given direction in a specific region of the space underground.

Last but not least, imaging techniques require the knowledge of a position to associate to each measurement point, whatever the scan path is, a regular grid or a manual scanning. A real time positioning system that provides the 3D position and orientation of the sensor is thus needed. A position accuracy of less than 1 cm is mandatory. We are currently developing a lightweight portable system based on a camera and an accelerometer [12]. The feasibility study is completed and a prototype will soon be available.

ACKNOWLEDGEMENT

7 REFERENCES

[1] C. E. Baum, Eds, "Detection and Identification of Visually Obscured Targets", Taylor & Francis, 1999.
[2] Y. Das et al, "Analysis of an Electromagnetic Induction Detector for Real-Time Location of Buried Objects", IEEE Trans. Geoscience and Remote Sensing., vol. 28, no.3, pp. 278-289, 1990.
[3] I. J. Won et al., "GEM3: a Monostatic Broadband Electromagnetic Induction Sensor", J. of Environmental and Engineering Geophysics, vol. 2, no.1, pp. 53-64, March 1997.
[4] P. Gao, L. Collins, "Improved Signal Processing Approaches for Landmine Detection", Proc. SPIE on Detection and Remediation Technologies for Mines and Minelike Targets III, vol. 3392, pp. 1034-43, 1998.
[5] A. Rosenfield, A. C. Kak, "Digital Picture Processing", Chap. 7, Academic Press, 1982.
[6] D. Daniels, "Surface-Penetrating Radar", IEE books, 1996.
[7] J. A. Stratton, "Electromagnetic theory", McGraw-Hill Book Company, 1941.
[8] G. Franceschetti, "Electromagnetics – Theory, Techniques, and Engineering Paradigms", Plenum Press, 1997.
[9] H.C. Andrews and B.R. Hunt, "Digital Image Restoration", Prentice Hall Inc., Englewood Cliffs, New Jersey, 1977.
[10] Guy Demoment. "Image reconstruction and restoration: Overview of common estimation structures and problem"s. IEEE Transactions on Acoustics, Speech and Signal Processing, vol. 37, no. 12, pp 2024-2036, December 1989.
[11] A. K. Katsaggelos. "Digital Image Restoration", Springer-Verlag, 1991.
[12] C. Beumier et al., "Motion estimation of a hand-held mine detector", Signal Processing Symposium, Hilvarenbeek, NL, 23-24th March 2000.